

Elliptically polarized attosecond pulse generation by corotating bicircular laser fieldsWenqing Li,¹ Xiaosong Zhu,^{1,*} Pengfei Lan,^{1,†} and Peixiang Lu^{1,2}¹*Wuhan National Laboratory for Optoelectronics and School of Physics, Huazhong University of Science and Technology, Wuhan 430074, China*²*Hubei Key Laboratory of Optical Information and Pattern Recognition, Wuhan Institute of Technology, Wuhan 430205, China*

(Received 26 November 2021; revised 30 August 2022; accepted 11 October 2022; published 24 October 2022)

We revisit high-order-harmonic generation (HHG) in corotating bicircular fields, which possess high optical chirality, and extend the study to a frequency ratio higher than 1:2. By analyzing the classical trajectories in the corotating bicircular fields in the rotating frame, we show that the Coriolis-force effect that hinders HHG decreases with the frequency ratio. Given these features, we propose a method for producing highly elliptically polarized attosecond pulses (with ellipticity up to $\epsilon = 0.88$) using the corotating bicircular field with a frequency ratio of 1:3. A comparison is also made with the extensively studied counter-rotating configurations with a frequency ratio of 1:2 considering various laser parameters. The results affirm the validity and superiority of the corotating configurations, from which both the ellipticity and yield of generated attosecond pulses are higher than those from the counter-rotating configurations.

DOI: [10.1103/PhysRevA.106.043115](https://doi.org/10.1103/PhysRevA.106.043115)**I. INTRODUCTION**

High-order-harmonic generation (HHG) in atoms and molecules is a highly nonlinear process in strong light-matter interactions [1–3]. It can be understood with the three-step model, including ionization, acceleration after liberation, and recombination of an electron in strong laser fields [4]. HHG represents one of the primary gateways to obtain tabletop extreme ultraviolet or soft x-ray attosecond light sources [5–9]. Meanwhile, it holds the promise to deepen or revolutionize our understanding of the fundamental dynamics of atoms [10,11], molecules [12–15], plasmas [16–18], and solids [19–21] on subfemtosecond and subangstrom scales. Therefore, HHG has been a hot topic in recent decades.

Due to the recombination characteristic of the HHG process, studies on HHG usually consider linearly polarized driving fields [22]. A linearly polarized driving field is one-dimensional, so its scope of application of HHG is greatly limited. To overcome this issue, driving fields with additional degrees of freedom have also been considered [23–28]. In 1995, Long *et al.* [29] proposed the bicircular laser field, which consists of two coplanar circularly polarized fields. Such a field has a huge parameter space: Intensities, helicities, frequency ratio, relative phase, etc. By adjusting these parameters, researchers can efficiently manipulate the two-dimensional (2D) strong-field-driven electron trajectories in the HHG process [30] and coherently control quantum states [31,32]. One of the major applications of HHG using bicircular fields is to generate elliptically polarized attosecond pulses [23,24,33], which can be used to study x-ray magnetic circular dichroism spectroscopy [24,34,35]. Furthermore, the bicircu-

lar fields are employed to generate high-order harmonics from chiral molecules (cHHG)[36–40], from which the chirality and ultrafast chiral dynamics of the gaseous target can be studied in an all-optical manner.

Notably, besides the features of the target system, the chiro-optical response, such as the ellipticity of the synthesized pulses and the circular dichroism of cHHG, is dependent on the chirality of the light [41–45]. Analogous to the chirality of matter, the chirality of light, as a fundamental concept of the electromagnetic field, describes the chiral geometrical picture, and it can be evaluated by a time-even pseudoscalar—the optical chirality (OC) [41,42,46]. To enhance the chiro-optical response, light with ultrahigh OC, called the “superchiral” field, has been used in linear chiral light-matter interactions [41,42,47].

In many works on HHG, bicircular fields whose two circularly polarized components have opposite helicities (i.e., are counter-rotating) and almost equal intensities are used. According to Ref. [48], the OC is proportional to the sum of the energy-weighted helicities of the circularly polarized components. Thus, it is intuitive to judge that the OC of a counter-rotating bicircular field is low [43], which will restrict its application as a chiral laser field. One direct way to obtain laser fields with high chirality is to superpose the two circularly polarized components with the same helicity, forming a corotating bicircular field. Recently, transverse anomalous-Hall-like currents, a chiral phenomenon in solids, were predicted in the corotating field [49], which implies its high chirality.

However, compared with research on HHG with counter-rotating bicircular fields [23,24,29,50–53], there are few studies on HHG with corotating bicircular fields [54,55]. The works considering corotating bicircular fields basically focused on a frequency ratio of 1:2. It is shown that HHG yield in the corotating bicircular field with such a frequency ratio is

*zhuxiaosong@hust.edu.cn

†pengfeilan@hust.edu.cn

significantly lower than that of the counter-rotating field [30]. The lower yield is explained in the rotating frame by the stronger Coriolis force effect in the former case than in the latter case, which inhibits the recombination of the ionized electrons [56,57].

In this work, we revisit HHG in the corotating bicircular fields and extend the study to a higher frequency ratio. By analyzing the electron dynamics in the corotating bicircular fields in the rotating frame, we found that the Coriolis-force effect decreases as the frequency ratio increases, although the Coriolis force becomes even stronger. The results suggest an advantageous corotating configuration to generate highly elliptically polarized attosecond pulses, which has seldom been studied before. Further, we propose a specific method for this application using the corotating bicircular field with a frequency ratio of 1:3. To clarify the validity and superiority of our method, we compare it with the extensively studied counter-rotating configurations with a frequency ratio of 1:2. The results affirm the superiority in ellipticity and yield of the synthesized attosecond pulse in our method. Finally, an extended comparison shows that the superiority of the corotating configurations remains for various total intensities and fundamental wavelengths.

II. THEORETICAL MODEL

A. Semiclassical model

The semiclassical model [58–60] is used to study the electron trajectories in the HHG process. For each trajectory, the tunneling electron is launched at ionization time t_i , with an initial transverse momentum p_\perp and a zero initial longitude momentum $p_\parallel = 0$. The initial position is set at the origin.

The evolution of the electron is governed by Newton's equation in the driving laser field. For the sake of simplicity, the effect of the Coulomb potential is neglected [30]. The weight of each trajectory contributing to HHG is

$$W(t_i, p_\perp) = w_t(t_i)w_p(p_\perp). \quad (1)$$

w_t is the ionization rate for electrons with zero initial momentum at t_i given by the Ammosov-Delone-Krainov model [61]. w_p is the dependence of the ionization rate on the electron initial momentum p_\perp [62], which can be written as

$$w_p(p_\perp) = \exp\left[-\frac{2(2I_p + p_\perp^2)^{3/2}}{3|E(t_i)|}\right]. \quad (2)$$

I_p is the ionization potential of the target atom. When the distance between the tunneling electron and parent ion is less than 1 a.u., the recombination occurs, and the corresponding moment is recombination time t_r . The recombination probability of each electron is written as $R(t_i, p_\perp) = W(t_i, p_\perp)\theta(t_i, p_\perp)$, where $\theta = 1$ means the recombination occurs and otherwise $\theta = 0$. Atomic units (a.u.) are used throughout this paper unless otherwise stated.

B. Quantum model

High-order-harmonic spectra are calculated by numerically solving the 2D single-active-electron time-dependent

Schrödinger equation (TDSE) [63]

$$i\frac{\partial\Psi(\mathbf{r}, t)}{\partial t} = H(\mathbf{r}, t)\Psi(\mathbf{r}, t). \quad (3)$$

$H(\mathbf{r}, t)$ is the Hamiltonian,

$$H(\mathbf{r}, t) = H_0 - \mathbf{r} \cdot \mathbf{E}(t) = -\frac{1}{2}\nabla^2 + V(\mathbf{r}) - \mathbf{r} \cdot \mathbf{E}(t). \quad (4)$$

H_0 is the field-free Hamiltonian. $V(\mathbf{r}) = -1/\sqrt{|\mathbf{r}|^2 + \alpha}$ is soft-core potential, and α is the soft-core parameter. In our calculation, the laser field is written as

$$\mathbf{E}(t) = f(t)\mathbf{E}_{\text{Bi}}(t). \quad (5)$$

$\mathbf{E}_{\text{Bi}}(t)$ represents the bicircular carrier wave. $f(t)$ is the envelope function of the laser pulse, which is trapezoidal, with a three-cycle rise, a three-cycle drop, and a four-cycle long flattop (in units of the optical cycle of the fundamental laser field).

The initial wave function is the s ground state obtained by the imaginary-time propagation. The 2D-TDSE is discretized on a Cartesian grid $L_x \times L_y$ for $L_x = L_y = 360$ a.u., with grid spacing $dx = dy = 0.12$ a.u., and propagated with the split-operator method [63] with a time step $dt = 0.04$ a.u. After each time step, the wave function is multiplied by a $\sin^{\frac{1}{8}}$ mask function that varies from 1 to 0 over a width of 45 a.u. at the inner boundary to avoid spurious reflections. Convergence has been tested for grid size and time step.

The time-dependent dipole acceleration can be obtained according to the Ehrenfest theorem

$$\mathbf{a}(t) = -\langle\Psi(\mathbf{r}, t)|\nabla V(\mathbf{r}) - \mathbf{E}(t)|\Psi(\mathbf{r}, t)\rangle. \quad (6)$$

Then, the harmonic spectrum is obtained from the Fourier transform of $\mathbf{a}(t)$,

$$E_{x,y}(q\omega) = \int a_{x,y}(t) \exp(-iq\omega t) dt, \quad (7)$$

where q denotes harmonic order and subscripts x and y represent the corresponding x and y components. The harmonic radiation can also be projected into two counter-rotating components, i.e., the right-circularly polarized component $E_+ = (E_x + iE_y)/\sqrt{2}$ and the left-circularly polarized component $E_- = (E_x - iE_y)/\sqrt{2}$. The intensities of the two components are $I_\pm = |E_\pm|^2$.

The ellipticity of the harmonics can be calculated by [64,65]

$$\epsilon = \frac{|E_+| - |E_-|}{|E_+| + |E_-|}. \quad (8)$$

The synthesized temporal pulse is obtained by inverse Fourier transformation of a specific range of harmonics. Its ellipticity is calculated by the ratio between the minor axis and the major axis of the pulse.

III. RESULTS AND DISCUSSION

A. Wave form of bicircular laser fields

The carrier wave of the bicircular laser field can be written as

$$\mathbf{E}_{\text{Bi}}(t) = \frac{1}{\sqrt{2}}E_0 \begin{bmatrix} \cos(\omega t) + \cos(n\omega t) \\ \sin(\omega t) - \sin(n\omega t) \end{bmatrix}. \quad (9)$$

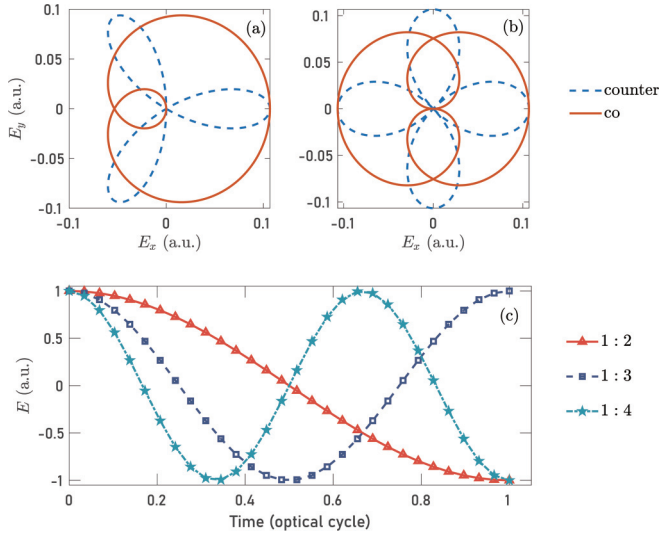


FIG. 1. Lissajous figures of bicircular laser fields with frequency ratios of (a) 1:2 and (b) 1:3. The orange solid lines depict the wave form of corotating bicircular fields, and the blue dotted lines show the wave form of counter-rotating ones. (c) Normalized linear field terms of the corotating bicircular fields in the rotating frame for different frequency ratios.

ω is the frequency of the fundamental laser pulse. n is an integer, and $|n|$ denotes the frequency ratio, where $n \geq 2$ corresponds to the counter-rotating fields and $n \leq -2$ represents the corotating fields. E_0 is the amplitude of each circularly polarized laser pulse. Here, the intensities of the two circularly polarized components are the same; that is, the intensity ratio is $I_{|n|}/I_1 = 1$. I_1 represents the intensity of the ω component, and $I_{|n|}$ is the intensity of the $n\omega$ component.

Equation (9) can be factorized and rewritten as

$$\mathbf{E}_{\text{Bi}}(t) = 2E_0 \cos\left(\frac{1+n}{2}\omega t\right) \begin{bmatrix} \cos\left(\frac{1-n}{2}\omega t\right) \\ \sin\left(\frac{1-n}{2}\omega t\right) \end{bmatrix}, \quad (10)$$

which indicates that the field can be viewed as a circularly polarized field with a carrier frequency of $|\frac{1-n}{2}\omega|$ and a time-varying amplitude modulated by $\cos(\frac{1+n}{2}\omega t)$ [see Fig. 1(c)].

The bicircular laser field possesses an s -fold dynamical symmetry with $s = |n + 1|$, which permits the emission of only $(sm \pm 1)$ -order harmonics ($m \in \mathbb{N}$). [26,66–68]. Lissajous figures of $\mathbf{E}_{\text{Bi}}(t)$ are displayed in Figs. 1(a) and 1(b) for frequency ratios of 1:2 and 1:3, respectively. One can see the respective one- to fourfold dynamical symmetries for the four cases.

B. Chirality of bicircular laser fields

The OC, characterizing the instantaneous chirality of light, can be given by $C = \frac{\epsilon_0}{2} \mathbf{E} \cdot \nabla \times \mathbf{E} + \frac{1}{2\mu_0} \mathbf{B} \cdot \nabla \times \mathbf{B}$ (in mks) [41,46]. Alternatively, Bliokh and Nori [48] derived an intuitive form of the OC in the helicity representation:

$$C = \frac{w}{c_0} \chi, \quad \chi = \frac{\bar{w}^+ - \bar{w}^-}{\bar{w}^+ + \bar{w}^-}. \quad (11)$$

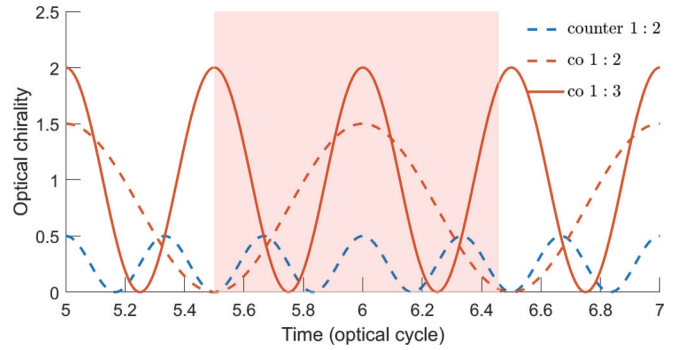


FIG. 2. Instantaneous OC of the bicircular fields. The blue dotted line denotes the counter-rotating field with a frequency ratio of 1:2. Orange lines represent the corotating bicircular fields with frequency ratios of 1:2 and 1:3. The light-orange area roughly represents the travel time of tunneling electrons in the HHG process in the corotating bicircular field with a frequency of ratio 1:3.

c_0 is the speed of light in vacuum. χ is called the chirality density. w is the total energy density of the laser field, and \bar{w} is its time averaging. \bar{w}^σ is the energy density of the σ -polarized part of the field, where $\sigma = +, -$ corresponds to the right- and left-circularly polarized components, respectively. Regarding the bicircular fields, Eq. (11) indicates that the OC of counter-rotating bicircular fields should be low, as the contributions of the right- and left-circularly polarized components will counteract each other. On the other hand, it immediately suggests that one can acquire laser fields with high chirality by superposing the circularly polarized components with the same helicity, i.e., synthesizing the corotating bicircular field.

To quantitatively evaluate the OC of the bicircular fields, one can follow Ref. [43], dividing OC into the polarization and orbital terms. In the case of HHG discussed in this work, the polarization term is dominant. Thus, the OC is calculated based on the polarization term:

$$C_p = \frac{\phi'(t)I(t)}{c_0\epsilon_0|E_0|^2\omega}, \quad (12)$$

where $I = (c_0\epsilon_0/2)|\mathbf{E}|^2 + (c_0/2\mu_0)|\mathbf{B}|^2$ is the light intensity, $\phi = \tan^{-1}(E_y/E_x)$ is the angle of the electric field vector, and ϕ' labels the time derivative of ϕ .

We numerically calculate the OC of the counter-rotating bicircular field with a frequency ratio of 1:2 and corotating bicircular fields with frequency ratios of 1:2 and 1:3, as shown in Fig. 2. The intensity ratio of these fields is $I_n/I_1 = 1$. Mostly, the instantaneous OC of the corotating bicircular field is greater than that of the counter-rotating field.

Assuredly, HHG is an extremely nonlinear noninstantaneous process, so one should consider noninstantaneous OC—the average value of the instantaneous OC experienced by the tunneling electrons [43,69]. For the counter-rotating bicircular field with a frequency ratio of 1:2, the instantaneous OC varies from 0 to 0.5, and the noninstantaneous value is less than 0.5. Considering the corotating field, we take the one with the frequency ratio of 1:3, for instance. The light-orange area in Fig. 2 roughly denotes the travel time (from t_i to t_r) of tunneling electrons in the HHG process, which is obtained with the semiclassical simulation described in Sec. II A. The

corresponding noninstantaneous value is around 1, which is larger than the maximum instantaneous OC of the counter-rotating bicircular field, as Fig. 2 shows. Similar results can also be obtained for other fields, showing the higher chirality of the corotating bicircular field than the counter-rotating field. Thus, one can expect that attosecond pulses with higher ellipticity can be obtained with corotating bicircular fields [43].

C. HHG process in bicircular laser fields

According to Eq. (10), it is instructive to analyze the HHG process in a rotating frame which rotates with the same angular frequency as the circularly polarized term. After performing a unitary transformation on the Hamiltonian [Eq. (4)] [70–73], the Hamiltonian $H'(t)$ in the rotating frame can be obtained:

$$H'(t) = H_0 + 2E_0 \cos\left(\frac{n+1}{2}\omega t\right) \hat{x}' + \frac{n-1}{2}\omega L_z. \quad (13)$$

The result generally shows that, in the rotating frame, the bicircular field corresponds to a linear field term $[2E_0 \cos(\frac{n+1}{2}\omega t)]$, in competition with a rotation angular momentum term $(\frac{n-1}{2}\omega L_z)$ responsible for the Coriolis force [56,57], where the x' axis is parallel to the linear term in the rotating frame and L_z is the angular momentum operator around the z axis. The linear field term is shown in Fig. 1(c). The Coriolis force is proportional to $\frac{n-1}{2}\omega$ and perpendicular to the instantaneous direction of the electron motion.

To unveil the HHG process and the HHG yield in the bicircular field, we analyze the electron trajectories in the rotating frame using the semiclassical model described in Sec. II A. As an example, a pair of trajectories is presented in Fig. 3(a). The driving field is the $\omega - 2\omega$ counter-rotating bicircular field with a fundamental wavelength of 800 nm. Its total intensity is $I = I_1 + I_2 = 4 \times 10^{14}$ W/cm². The solid line represents the trajectory with the highest recombination probability $R(t_i, p_\perp)$, whose corresponding tunneling electron is launched at the peak of the driving field with $p_\perp = 0.46$ a.u. The dashed line shows the trajectory for a tunneling electron with zero initial momentum, and other conditions are the same as those for the solid line. One can see that the trajectory gains a large lateral offset L_{off} , as indicated by the black asterisk, which is caused by the nonzero Coriolis force. Therefore, electrons with zero initial momentum can hardly return to the parent ion, and high-order harmonics cannot be generated, as shown by the dashed line in Fig. 3(a) [22]. However, if the electron is launched with a finite initial transverse momentum, a return can be achieved, as shown by the solid line in Fig. 3(a).

Besides the Coriolis force, L_{off} is also closely related to the travel time in the external field. For simplicity, we first consider a simple case where the Coriolis term is much weaker than the linear term, so that the linear term dominates the electron motion and the instantaneous direction of the electron motion is basically along the linear field term (x' axis) in the rotating frame. Namely, one can approximate that the Coriolis force is perpendicular to the x' axis. In this case, considering the motion along a straight line with zero initial displacement and velocity, one can estimate that L_{off} is proportional to the

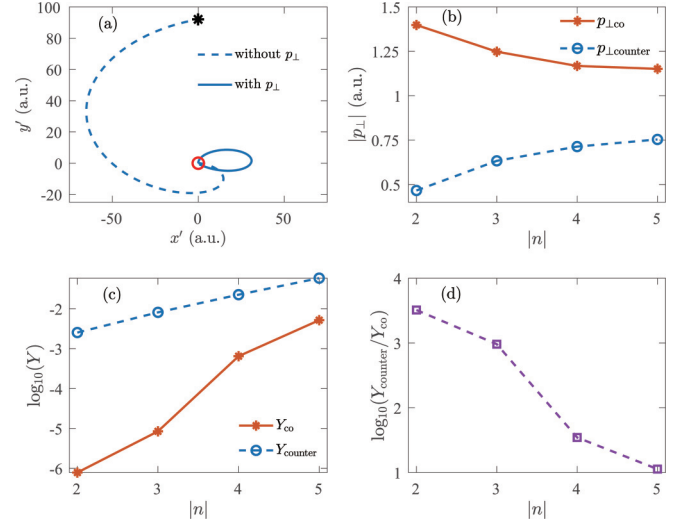


FIG. 3. (a) Representative classical trajectories in the rotating frame. The solid line displays the representative trajectory in the counter-rotating bicircular field with a frequency ratio of 1:2 (see the text). The conditions of the dashed line are the same as those for the solid line, except for a zero initial transverse momentum $p_\perp = 0$. The red circle denotes the parent ion where ionization occurs. The black asterisk represents the position where the dashed line returns to $x' = 0$. (b) Initial transverse momentum of typical trajectories. (c) HHG yield in bicircular fields calculated by TDSE. (d) The ratios of HHG yield in the counter-rotating bicircular field to that in the corotating bicircular field with the same frequency ratio. The target atom is He.

Coriolis force and square of the travel time τ (proportional to the period of the linear field term):

$$L_{\text{off}} \propto \left| \frac{n-1}{2}\omega \right| \tau^2. \quad (14)$$

In order to guarantee the recombination, a nonzero p_\perp is required to overcome the nonzero lateral offset:

$$p_\perp \propto \frac{L_{\text{off}}}{\tau} = \frac{|n-1|}{2}\omega\tau. \quad (15)$$

The absolute value of p_\perp indicates the ability of the Coriolis force to hinder the recombination and generation of high harmonics. According to Eq. (13), one can obtain

$$\tau \propto \left| \frac{2\pi}{\frac{n+1}{2}\omega} \right| = \frac{4\pi}{|n+1|\omega}, \quad (16)$$

which decreases as the frequency ratio increases, as shown in Fig. 1(c). Thus, one finally gets

$$p_\perp \propto \left| \frac{n-1}{n+1} \right|. \quad (17)$$

Equation (17) indicates that, as the frequency ratio increases, the required p_\perp increases for the counter-rotating bicircular fields ($n \geq 2$) but decreases for the corotating ($n \leq -2$) fields. Therefore, for the corotating fields, the Coriolis effect hindering the HHG decreases as the frequency ratio increases, which will contribute to considerable HHG yield using a high frequency ratio.

The above analysis indicates the trend of the HHG yield with the change in $|n|$, although it is based on the approximation that the Coriolis term is much smaller than the linear term. For the generally applied laser parameters, this condition is often not well satisfied. To more rigorously verify our analysis, we numerically calculate the recombination electron trajectories in the bicircular laser fields in the rotating frame with the semiclassical model, as described in Sec. II A. Without loss of generality, we consider the fundamental laser wavelength $\lambda = 800$ nm, the total intensity of the bicircular field $I = I_1 + I_n = 4 \times 10^{14}$ W/cm², and the intensity ratio fixed to $I_n/I_1 = 1$. We calculate the family of recombination trajectories associated with the plateau regime and pick the trajectory with the highest recombination probability $R(t_i, p_\perp)$ from them as the representative trajectories. The $|p_\perp|$ of the representative trajectories is shown in Fig. 3(b). The result shows that the trend of $|p_\perp|$ is the same as Eq. (17) predicts. Since $|p_\perp|$ of other recombination trajectories associated with the plateau regime around the representative trajectories show the same tendency, it is valid and concise to reflect the related physics by showing only the representative trajectories.

As shown in Fig. 3(c), we further calculate the HHG yield Y induced by the bicircular fields as a function of frequency ratio $|n|$ using TDSE described in Sec. II B. The target atom is He. The HHG yield Y is evaluated by averaging permitted harmonics in the plateau region from I_p to the cutoff energy [56]. To match its ionization potential, the soft-core parameter is chosen to be 0.0693. Figure 3(c) illustrates the increasing trend of the HHG yield in both the counter- and corotating bicircular fields as the frequency ratio increases. This is because the ionization rate w_i increases as the frequency ratio increases. Nevertheless, the slope of the yield for the corotating field is larger than the counter-rotating case, so the yield for the former increases and approaches that of the latter quickly. The different slopes result from the different trends of the Coriolis effect hindering the recombination determined by the wave form of driving fields, as shown in Fig. 3(b). To intuitively shed light on the effect caused by the wave form of the laser fields, we show the ratios of HHG yield $Y_{\text{counter}}/Y_{\text{co}}$ generated by the counter-rotating bicircular field to that of the corotating one with the same frequency ratio in Fig. 3(d). One can see that when the frequency ratio changes from 2 to 5, the HHG yield ratio $Y_{\text{counter}}/Y_{\text{co}}$ changes from $10^{3.5}$ to 10^1 . This sharp decrease unambiguously supports the prediction about the Coriolis force effect of co- and counter-rotating driving fields from Eqs. (14)–(17) and the semiclassical simulation for Fig. 3(b). The results imply that one may obtain a laser field with high chirality and considerable HHG efficiency by employing the corotating bicircular fields with a high frequency ratio.

In this section, we outline the conclusion that the Coriolis effect hindering the HHG decreases for corotating bicircular fields but increases for the counter-rotating bicircular fields with the frequency ratio. Regarding this conclusion, a fixed intensity ratio ($I_n/I_1 = 1$) is used. However, this fixed intensity ratio is not beneficial in the application to generate an elliptically polarized attosecond pulse. For example, the attosecond pulse induced by the $\omega - 2\omega$ counter-rotating configurations with intensity ratio $I_2/I_1 = 1$ is nearly linear [33,35,43] and cannot be used directly to generate the elliptically polarized

attosecond pulse. In general, to produce the elliptically polarized attosecond pulse, one has to tune the intensity ratio, and the corresponding efficiency drops dramatically [33]. Thus, for this application, it is not instructive to consider the relative yield of the pulse between the corotating and counter-rotating configurations with the fixed intensity ratio $I_n/I_1 = 1$. Conversely, to examine the results for such an application, appropriate intensity ratios for the respective configurations should be considered in specific schemes, as in the next section.

D. Elliptically polarized attosecond pulse generation

Utilizing the large-optical-chirality feature of the corotating field with a high frequency ratio, we propose a method for producing highly elliptically polarized attosecond pulses from He using the $\omega - 3\omega$ corotating field with the optimized intensity ratio I_3/I_1 . The fundamental wavelength is 800 nm, and the total intensity is $I = I_1 + I_3 = 4 \times 10^{14}$ W/cm². The HHG is simulated using TDSE, as described in Sec. II B. In Fig. 4, we present simulation results for the logarithm of the harmonic intensity [Fig. 4(a)] and the ellipticity of permitted harmonics [Fig. 4(b)] in false color as a function of the intensity ratio and the harmonic order. The intensity ratio changes from 0.2 to 4. Roughly, as shown in Fig. 4(a), the HHG yield increases for the higher intensity ratio. In addition, Fig. 4(b) shows that an intensity ratio higher than 1 promises higher ellipticity in the near-cutoff region than that for $I_3/I_1 = 1$. To identify the optimized intensity ratio, we calculate the ellipticity of the temporal pulses synthesized with near-cutoff harmonics from a spectral range with a fixed width of 0.855 a.u. for different intensity ratios. The central frequency of the spectral range is adjustable for the highest ellipticity. The ellipticity of pulses for each given laser parameter (intensity ratio here) is represented by that of the strongest pulse [e.g., as denoted by the cyan-blue region in Fig. 4(d)] in one optical cycle corresponding to the flattop range of the trapezoidal driving pulse. We find the optimized intensity ratio $I_3/I_1 = 3.6$ for the highest ellipticity of generated pulses. The corresponding HHG spectra (the red and black lines) are displayed in Fig. 4(c). The synthesized temporal pulses are shown in Fig. 4(d). The ellipticity is as high as 0.88, and the duration is around 645 as.

In experiments, the intensity of the field varies in the focal region. So the results from focal averaging over the intensity, following Refs. [74,75], are also shown in Fig. 4(c). The propagation effects are not considered. We suppose that the laser field can be described by a Gaussian beam. The peak intensity is chosen to be $I_0 = 4 \times 10^{14}$ W/cm². As shown in Fig. 4(c), although an obvious difference between the results with and without the focal averaging is seen for the low-order harmonics, the near-cutoff harmonics are basically the same. Since we focus on the near-cutoff harmonics here, considering the focal averaging over the laser intensity does not significantly affect our method. Thus, for the results discussed below, the focal averaging is not included.

Next, to further clarify the validity and superiority of our method, we compare the corotating configuration with the single-color linear configuration and the extensively studied $\omega - 2\omega$ counter-rotating configuration [33,74,76]. Following

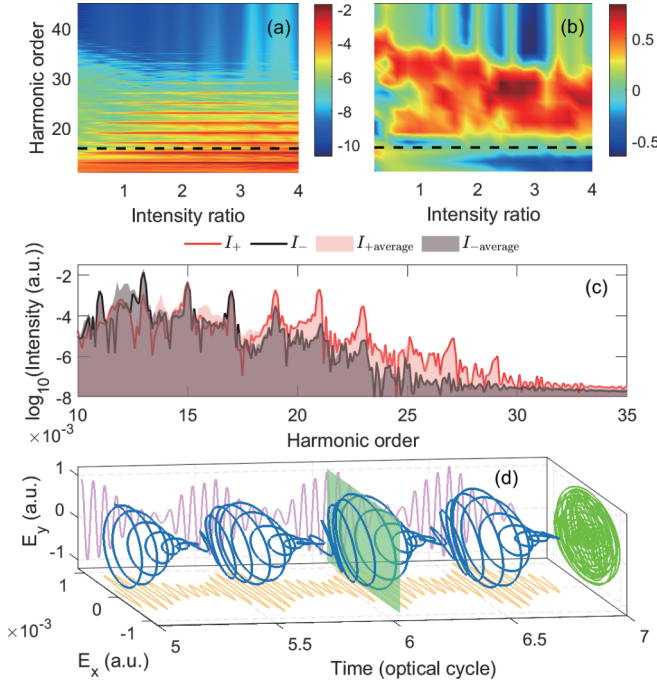


FIG. 4. Logarithm of (a) the harmonic intensity and (b) the ellipticity of permitted harmonics for HHG by a He atom and $\omega - 3\omega$ corotating bicircular field with a fundamental wavelength of 800 nm. The results are presented in false color as a function of the intensity ratio (I_3/I_1) and the harmonic order. The total intensity is fixed to $I = 4 \times 10^{14}$ W/cm². The dashed lines mark the ionization energy I_p . (c) The spectra of the right-circularly polarized harmonics (red solid line) and the left-circularly polarized harmonics (black solid line) for intensity ratio $I_3/I_1 = 3.6$. The red (dark gray) shaded region represents the corresponding right- (left-) circularly polarized harmonics by focal averaging over the laser intensity with the peak intensity $I_0 = 4 \times 10^{14}$ W/cm². For the convenience of comparison, the spectra after focal averaging over the laser intensity are shifted by a constant factor. (d) Three-dimensional plot of the electric field of synthesized elliptically polarized pulses. The pulses are obtained by synthesizing high-order harmonics denoted by the solid lines in (c). The corresponding spectral width is 0.855 a.u. (from 18th-order to the 33rd-order harmonics).

Ref. [33], the intensity ratio of the $\omega - 2\omega$ counter-rotating configuration is fixed to $I_2/I_1 = 0.1$ to achieve high ellipticity of generated attosecond pulses. All the other conditions of the three configurations (e.g., total intensity, fundamental wavelength, and target atom) are the same as those for Fig. 4. We still choose the harmonics near the cutoff in the spectral range with a fixed width of 0.855 a.u. to guarantee an approximately equal pulse duration. For the counter-rotating configuration, the central frequency of the chosen range is adjustable to get the highest ellipticity too. Complementarily, the spectral range in the linear configuration is consistent with the corotating one. The ellipticity of the temporal pulses for different configurations is obtained in the same way as for Fig. 4. The yield of synthesized pulses is evaluated by integrating the intensity spectrum of the high harmonics in the chosen spectral range.

The ellipticity and yield of synthesized pulses are summarized in Fig. 5 (dark-blue diamond, circle, and asterisk). One can see that the yield of pulses from the corotating

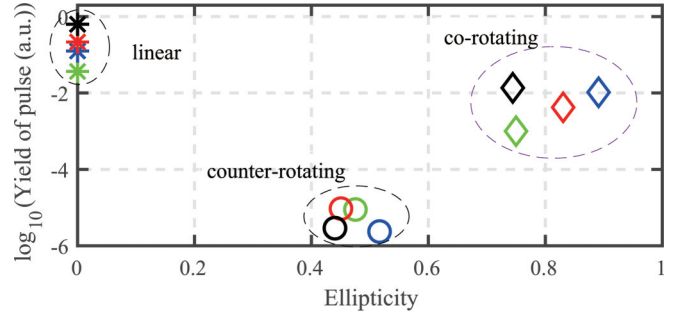


FIG. 5. The ellipticity of elliptically polarized pulses and the corresponding yield induced by three configurations for total intensities of 3×10^{14} W/cm² (green), 4×10^{14} W/cm² (dark blue), 5×10^{14} W/cm² (red), and 6×10^{14} W/cm² (black). The diamonds, circles, and asterisks represent the corotating, counter-rotating, and linear configurations, respectively. The target atom is He, and the fundamental wavelength is fixed to 800 nm.

configurations is only one order lower than that in the linear field (comparing the dark-blue diamond and asterisk in Fig. 5). Meanwhile, the ellipticity of synthesized pulses from the counter-rotating configuration is only 0.52, which is approximately consistent with the simulation in Ref. [33]. The ellipticity in the corotating case (dark-blue diamond) is much higher than the ellipticity that can be reached in the counter-rotating case (dark-blue circle) due to the much higher optical chirality of the corotating field, and the yield of the pulse from the corotating configurations is a few orders higher than the counter-rotating one. Increasing the frequency ratio from 1:2 to 1:3 not only increases the ionization rate but also increases the probability of recombination by decreasing the Coriolis effect in the corotating configuration. Both effects contribute to the considerable yield of the synthesized pulse.

Note that the proposed method considers only an atomic s state as the target. The obtained ellipticity of 0.88 is higher than most results from atoms in a collinear geometry [33,74,76–78]. Our method can be further optimized to obtain higher ellipticity by utilizing molecular or current-carrying states [79,80].

For the wider parameter space, we vary the total intensity and the fundamental wavelength of the driving laser for the three configurations. For the corotating configurations, the intensity ratio is optimized to obtain the highest ellipticity. The intensity ratio of the counter-rotating configurations is fixed to $I_2/I_1 = 0.1$. The results from following the above procedure are summarized in Figs. 5 and 6. Figure 5 shows that the results under various total intensities are concentrated for both corotating and counter-rotating configurations. As shown in Fig. 6, with the fundamental wavelength increasing, the ellipticity and intensity of synthesized pulses decrease for both the bicircular configurations. However, for all the different given laser parameters in Figs. 5 and 6, the superiority of the corotating configurations holds: Both the ellipticity and intensity of synthesized pulses from the corotating configuration are higher than the corresponding results of the counter-rotating configuration. This can be understood from the fact that the wave form of the driving field is independent of the total intensity and fundamental wavelength of the driving field.

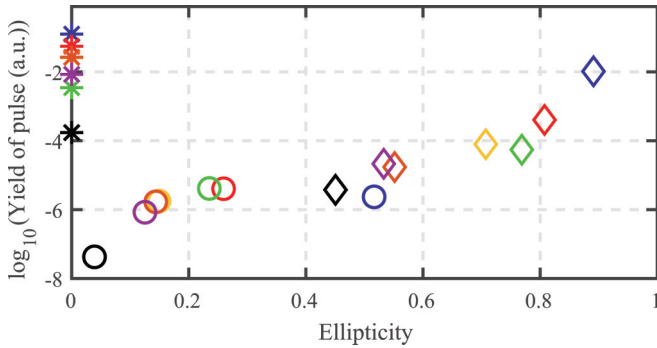


FIG. 6. The ellipticity of elliptically polarized pulses and the corresponding yield induced by three configurations for fundamental wavelengths of 800 nm (dark blue), 900 nm (red), 1000 nm (green), 1100 nm (yellow), 1200 nm (orange), 1300 nm (purple), and 1600 nm (black). The diamonds, circles, and asterisks represent the corotating, counter-rotating, and linear configurations, respectively. The target atom is He, and the total intensity is fixed to 4×10^{14} W/cm².

Thus, the advantageous features of the corotating field with a high frequency ratio determined by the wave form, such as the high optical chirality and weakened Coriolis effect, remain the same (if we ignore the Coulomb effect).

In this work, the wave-form effect of the corotating bicircular field in HHG is investigated; thus, a multicycle driving pulse is applied. Changing the length of the pulse of the driving laser will not affect the major results, as long as the driving field can be considered multicycle, because the wave form of the driving field does not change. As for the few-cycle case, due to the short pulse duration, there may not even be a complete wave form of a corotating bicircular field. The wave form of the bicircular field and the corresponding HHG may change significantly with the carrier envelope phases (CEPs) [81]. It would be more complicated to establish an intuitive relation between the results and driving laser with different CEPs. Thus, the effect of pulse length

on the results is not discussed in this work. Considering the multicycle bicircular laser, changing the relative phase of the two circularly polarized components leads to only a rotation of the overall wave form [55]. Thus, for atomic targets, the relative phase has no influence on the intensity and ellipticity of the high-order harmonics and synthesized pulses.

IV. CONCLUSION

In summary, we studied HHG driven by the corotating bicircular field, whose chirality is much larger than the corresponding counter-rotating one. By performing a classical trajectory analysis in the rotating frame, we found that the Coriolis force effect in the corotating bicircular field, which hinders the recombination of ionized electrons, decreases with the increase of the frequency ratio. Further, we proposed a method for producing highly elliptically polarized attosecond pulses using the $\omega - 3\omega$ corotating bicircular field. We also investigated the fundamental wavelength and intensity dependence of the $\omega - 3\omega$ corotating bicircular configurations and compared them with the extensively studied $\omega - 2\omega$ counter-rotating configurations. The larger ellipticity and higher yield of elliptically polarized attosecond pulses induced by the corotating configurations than those from the counter-rotating configurations unambiguously verify the validity and superiority of the corotating configurations.

ACKNOWLEDGMENTS

This work was supported by the Science and Technology Planning Project of Guangdong Province (Grant No. 2018B090944001), the National Key Research and Development Program (Grant No. 2019YFA0308300), and the National Natural Science Foundation of China (NSFC; Grants No. 12174134, No. 11774109, No. 12021004, and No. 91950202). The computation was completed on the HPC Platform of the Huazhong University of Science and Technology.

- [1] P. B. Corkum and F. Krausz, *Nat. Phys.* **3**, 381 (2007).
- [2] F. Krausz and M. Ivanov, *Rev. Mod. Phys.* **81**, 163 (2009).
- [3] H. Niikura and P. B. Corkum, in *Attosecond and Angstrom Science*, edited by P. R. Berman, C. C. Lin, and E. Arimondo, Advances in Atomic Molecular and Optical Physics (Elsevier Inc., 2007), Vol. 54, pp. 511–548.
- [4] P. B. Corkum, *Phys. Rev. Lett.* **71**, 1994 (1993).
- [5] T. Popmintchev, M.-C. Chen, P. Arpin, M. M. Murnane, and H. C. Kapteyn, *Nat. Photonics* **4**, 822 (2010).
- [6] E. J. Takahashi, P. Lan, O. D. Mücke, Y. Nabekawa, and K. Midorikawa, *Nat. Commun.* **4**, 2691 (2013).
- [7] A. Ferré, C. Handschin, M. Dumergue, F. Burgy, A. Comby, D. Descamps, B. Fabre, G. A. Garcia, R. Généaux, L. Merceron, E. Mével, L. Nahon, S. Petit, B. Pons, D. Staedter, S. Weber, T. Ruchon, V. Blanchet, and Y. Mairesse, *Nat. Photonics* **9**, 93 (2015).
- [8] T. Gaumnitz, A. Jain, Y. Pertot, M. Huppert, I. Jordan, F. Ardana-Lamas, and H. J. Wörner, *Opt. Express* **25**, 27506 (2017).
- [9] J. Li, X. Ren, Y. Yin, K. Zhao, A. Chew, Y. Cheng, E. Cunningham, Y. Wang, S. Hu, Y. Wu, M. Chini, and Z. Chang, *Nat. Commun.* **8**, 186 (2017).
- [10] A. D. Shiner, B. E. Schmidt, C. Trallero-Herrero, H. J. Wörner, S. Patchkovskii, P. B. Corkum, J.-C. Kieffer, F. Légaré, and D. M. Villeneuve, *Nat. Phys.* **7**, 464 (2011).
- [11] D. Azoury, O. Kneller, S. Rozen, B. D. Bruner, A. Clergerie, Y. Mairesse, B. Fabre, B. Pons, N. Dudovich, and M. Krüger, *Nat. Photonics* **13**, 54 (2019).
- [12] J. Itatani, J. Levesque, D. Zeidler, H. Niikura, H. Pépin, J. C. Kieffer, P. B. Corkum, and D. M. Villeneuve, *Nature (London)* **432**, 867 (2004).
- [13] S. Baker, J. S. Robinson, C. A. Haworth, H. Teng, R. A. Smith, C. C. Chirila, M. Lein, J. W. G. Tisch, and J. P. Marangos, *Science* **312**, 424 (2006).
- [14] O. Smirnova, Y. Mairesse, S. Patchkovskii, N. Dudovich, D. Villeneuve, P. Corkum, and M. Y. Ivanov, *Nature (London)* **460**, 972 (2009).

- [15] P. M. Kraus, B. Mignolet, D. Baykusheva, A. Rupenyanyan, L. Horný, E. F. Penka, G. Grassi, O. I. Tolstikhin, J. Schneider, F. Jensen, L. B. Madsen, A. D. Bandrauk, F. Remacle, and H. J. Wörner, *Science* **350**, 790 (2015).
- [16] P. Salières, L. L. Déroff, T. Auguste, P. Monot, P. dOliveira, D. Campo, J.-F. Hergott, H. Merdji, and B. Carré, *Phys. Rev. Lett.* **83**, 5483 (1999).
- [17] Z.-Y. Chen, *Phys. Rev. E* **97**, 043202 (2018).
- [18] M. A. Fareed, V. V. Strelkov, N. Thiré, S. Mondal, B. E. Schmidt, F. Légaré, and T. Ozaki, *Nat. Commun.* **8**, 16061 (2017).
- [19] S. Ghimire, A. D. DiChiara, E. Sistrunk, P. Agostini, L. F. DiMauro, and D. A. Reis, *Nat. Phys.* **7**, 138 (2011).
- [20] B. Zaks, R. B. Liu, and M. S. Sherwin, *Nature (London)* **483**, 580 (2012).
- [21] L. Li, P. Lan, X. Zhu, T. Huang, Q. Zhang, M. Lein, and P. Lu, *Phys. Rev. Lett.* **122**, 193901 (2019); L. Li, T. Huang, P. Lan, J. Li, Y. Zhang, X. Zhu, L. He, W. Cao, and P. Lu, *ibid.* **128**, 027401 (2022).
- [22] M. Möller, Y. Cheng, S. D. Khan, B. Zhao, K. Zhao, M. Chini, G. G. Paulus, and Z. Chang, *Phys. Rev. A* **86**, 011401(R) (2012).
- [23] A. Fleischer, O. Kfir, T. Diskin, P. Sidorenko, and O. Cohen, *Nat. Photonics* **8**, 543 (2014).
- [24] O. Kfir, P. Grychtol, E. Turgut, R. Knut, D. Zusin, D. Popmintchev, T. Popmintchev, H. Nembach, J. M. Shaw, A. Fleischer, H. Kapteyn, M. Murnane, and O. Cohen, *Nat. Photonics* **9**, 99 (2015).
- [25] G. Lambert, B. Vodungbo, J. Gautier, B. Mahieu, V. Malka, S. Sebban, P. Zeitoun, J. Luning, J. Perron, A. Andreev, S. Stremoukhov, F. Ardana-Lamas, A. Dax, C. P. Hauri, A. Sardinha, and M. Fajardo, *Nat. Commun.* **6**, 6167 (2015).
- [26] O. Neufeld, D. Podolsky, and O. Cohen, *Nat. Commun.* **10**, 405 (2019).
- [27] N. Sun, X. Zhu, B. Wang, D. Wang, R. Shao, P. Lan, and P. Lu, *Phys. Rev. A* **101**, 053437 (2020).
- [28] X.-S. Kong, H. Liang, X.-Y. Wu, and L.-Y. Peng, *J. Phys. B* **54**, 124004 (2021).
- [29] S. Long, W. Becker, and J. K. McIver, *Phys. Rev. A* **52**, 2262 (1995).
- [30] D. B. Milošević, W. Becker, and R. Kopold, *Phys. Rev. A* **61**, 063403 (2000).
- [31] M. S. Mrudul, Á. Jiménez-Galán, M. Ivanov, and G. Dixit, *Optica* **8**, 422 (2021).
- [32] X. Zhu, P. Lu, and M. Lein, *Phys. Rev. Lett.* **128**, 030401 (2022).
- [33] K. M. Dorney, J. L. Ellis, C. Hernández-García, D. D. Hickstein, C. A. Mancuso, N. Brooks, T. Fan, G. Fan, D. Zusin, C. Gentry, P. Grychtol, H. C. Kapteyn, and M. M. Murnane, *Phys. Rev. Lett.* **119**, 063201 (2017).
- [34] D. D. Hickstein, F. J. Dollar, P. Grychtol, J. L. Ellis, R. Knut, C. Hernández-García, D. Zusin, C. Gentry, J. M. Shaw, T. Fan, K. M. Dorney, A. Becker, A. Jaroń-Becker, H. C. Kapteyn, M. M. Murnane, and C. G. Durfee, *Nat. Photonics* **9**, 743 (2015).
- [35] T. Fan *et al.*, *Proc. Natl. Acad. Sci. USA* **112**, 14206 (2015).
- [36] R. Cireasa, A. E. Boguslavskiy, B. Pons, M. C. H. Wong, D. Descamps, S. Petit, H. Ruf, N. Thiré, A. Ferré, J. Suarez, J. Higué, B. E. Schmidt, A. F. Alharbi, F. Légaré, V. Blanchet, B. Fabre, S. Patchkovskii, O. Smirnova, Y. Mairesse, and V. R. Bhardwaj, *Nat. Phys.* **11**, 654 (2015).
- [37] O. Smirnova, Y. Mairesse, and S. Patchkovskii, *J. Phys. B* **48**, 234005 (2015).
- [38] D. Ayuso, P. Declava, S. Patchkovskii, and O. Smirnova, *J. Phys. B* **51**, 06LT01 (2018).
- [39] D. Baykusheva and H. J. Wörner, *Phys. Rev. X* **8**, 031060 (2018).
- [40] Y. Harada, E. Haraguchi, K. Kaneshima, and T. Sekikawa, *Phys. Rev. A* **98**, 021401(R) (2018).
- [41] Y. Tang and A. E. Cohen, *Phys. Rev. Lett.* **104**, 163901 (2010).
- [42] Y. Tang and A. E. Cohen, *Science* **332**, 333 (2011).
- [43] O. Neufeld and O. Cohen, *Phys. Rev. Lett.* **120**, 133206 (2018).
- [44] D. Ayuso, O. Neufeld, A. F. Ordonez, P. Declava, G. Lerner, O. Cohen, M. Ivanov, and O. Smirnova, *Nat. Photonics* **13**, 866 (2019).
- [45] O. Neufeld, M. Even Tzur, and O. Cohen, *Phys. Rev. A* **101**, 053831 (2020).
- [46] D. M. Lipkin, *J. Math. Phys.* **5**, 696 (1964).
- [47] E. Hendry, T. Carpy, J. Johnston, M. Popland, R. V. Mikhaylovskiy, A. J. Laphorn, S. M. Kelly, L. D. Barron, N. Gadegaard, and M. Kadodwala, *Nat. Nanotechnol.* **5**, 783 (2010).
- [48] K. Y. Bliokh and F. Nori, *Phys. Rev. A* **83**, 021803(R) (2011).
- [49] O. Neufeld, N. Tancogne-Dejean, U. De Giovannini, H. Hübener, and A. Rubio, *Phys. Rev. Lett.* **127**, 126601 (2021).
- [50] D. Baykusheva, M. S. Ahsan, N. Lin, and H. J. Wörner, *Phys. Rev. Lett.* **116**, 123001 (2016).
- [51] D. M. Reich and L. B. Madsen, *Phys. Rev. Lett.* **117**, 133902 (2016).
- [52] S. Odžak, E. Hasović, and D. B. Milošević, *Phys. Rev. A* **94**, 033419 (2016).
- [53] D. Wang, X. Zhu, H. Yuan, P. Lan, and P. Lu, *Phys. Rev. A* **101**, 023406 (2020).
- [54] Y. Qiao, D. Wu, J.-G. Chen, J. Wang, F.-M. Guo, and Y.-J. Yang, *Phys. Rev. A* **100**, 063428 (2019).
- [55] D. B. Milošević and W. Becker, *Phys. Rev. A* **102**, 023107 (2020).
- [56] A. D. Bandrauk, F. Mauger, and K.-J. Yuan, *J. Phys. B* **49**, 23LT01 (2016).
- [57] A. D. Bandrauk, J. Guo, and K.-J. Yuan, *J. Opt.* **19**, 124016 (2017).
- [58] L.-B. Fu, J. Liu, J. Chen, and S.-G. Chen, *Phys. Rev. A* **63**, 043416 (2001).
- [59] K. Doblhoff-Dier, K. I. Dimitriou, A. Staudte, and S. Gräfe, *Phys. Rev. A* **88**, 033411 (2013).
- [60] X. Zhu, X. Liu, Y. Li, M. Qin, Q. Zhang, P. Lan, and P. Lu, *Phys. Rev. A* **91**, 043418 (2015).
- [61] M. V. Ammosov, N. B. Delone, and V. P. Krainov, *Sov. Phys. JETP* **64**, 1191 (1986).
- [62] N. B. Delone and V. P. Krainov, *J. Opt. Soc. Am. B* **8**, 1207 (1991).
- [63] M. D. Feit, J. Fleck, Jr., and A. Steiger, *J. Comput. Phys.* **47**, 412 (1982).
- [64] C. Chen, Z. Tao, C. Hernández-García, P. Matyba, A. Carr, R. Knut, O. Kfir, D. Zusin, C. Gentry, P. Grychtol, O. Cohen, L. Plaja, A. Becker, A. Jaron-Becker, H. Kapteyn, and M. Murnane, *Sci. Adv.* **2**, e1501333 (2016).
- [65] X. Zhang, X. Zhu, X. Liu, D. Wang, Q. Zhang, P. Lan, and P. Lu, *Opt. Lett.* **42**, 1027 (2017).

- [66] O. E. Alon, V. Averbukh, and N. Moiseyev, *Phys. Rev. Lett.* **80**, 3743 (1998).
- [67] X. Liu, X. Zhu, L. Li, Y. Li, Q. Zhang, P. Lan, and P. Lu, *Phys. Rev. A* **94**, 033410 (2016).
- [68] E. Hasović, S. Odžak, W. Becker, and D. Milošević, *Mol. Phys.* **115**, 1750 (2017).
- [69] E. Bloch, S. Larroque, S. Rozen, S. Beaulieu, A. Comby, S. Beauvarlet, D. Descamps, B. Fabre, S. Petit, R. Taïeb, A. J. Uzan, V. Blanchet, N. Dudovich, B. Pons, and Y. Mairesse, *Phys. Rev. X* **11**, 041056 (2021).
- [70] A. D. Bandrauk and H. Z. Lu, *Phys. Rev. A* **68**, 043408 (2003).
- [71] K.-J. Yuan and A. D. Bandrauk, *Phys. Rev. A* **92**, 063401 (2015).
- [72] D. M. Reich and L. B. Madsen, *Phys. Rev. A* **93**, 043411 (2016).
- [73] D. Wang, X. Zhu, L. Li, X. Zhang, X. Liu, P. Lan, and P. Lu, *Phys. Rev. A* **98**, 053410 (2018).
- [74] D. B. Milošević, *Phys. Rev. A* **98**, 033405 (2018).
- [75] D. B. Milošević, *Opt. Express* **30**, 12163 (2022).
- [76] A. Jiménez-Galán, N. Zhavoronkov, D. Ayuso, F. Morales, S. Patchkovskii, M. Schloz, E. Pisanty, O. Smirnova, and M. Ivanov, *Phys. Rev. A* **97**, 023409 (2018).
- [77] L. Medišauskas, J. Wragg, H. van der Hart, and M. Y. Ivanov, *Phys. Rev. Lett.* **115**, 153001 (2015).
- [78] P.-C. Huang, C. Hernández-García, J.-T. Huang, P.-Y. Huang, L. Rego, C.-H. Lu, S.-D. Yang, L. Plaja, A. H. Kung, and M.-C. Chen, *IEEE J. Sel. Top. Quantum Electron.* **25**, 8800312 (2019).
- [79] X. Xie, A. Scrinzi, M. Wickenhauser, A. Baltuška, I. Barth, and M. Kitzler, *Phys. Rev. Lett.* **101**, 033901 (2008).
- [80] X. Zhang, X. Zhu, X. Liu, F. Wang, M. Qin, Q. Liao, and P. Lu, *Phys. Rev. A* **102**, 033103 (2020).
- [81] E. Goulielmakis, M. Schultze, M. Hofstetter, V. S. Yakovlev, J. Gagnon, M. Uiberacker, A. L. Aquila, E. M. Gullikson, D. T. Attwood, R. Kienberger, F. Krausz, and U. Kleineberg, *Science* **320**, 1614 (2008).